JGR Earth Surface

RESEARCH ARTICLE
10.1029/2021JF006382

Reanalysis of Polythermal Glacier Thermal Structure Using Radar Diffraction Focusing

Richard Delf[1,2], Robert G. Bingham[1], Andrew Curtis[1], Satyan Singh[1], Antonios Giannopoulos[3], Benjamin Schwarz[4], and Chris P. Borstad[5]

[1]School of GeoSciences, University of Edinburgh, Edinburgh, UK, [2]Department of Arctic Geology, University Centre in Svalbard, Longyearbyen, Norway, [3]School of Engineering, University of Edinburgh, Edinburgh, UK, [4]GFZ German Research Centre for Geosciences, Potsdam, Germany, [5]Norm Asbjornson College of Engineering, Montana State University, Bozeman, MT, USA

Abstract Ground-penetrating radar (GPR) is widely used on polythermal glaciers to image bed topography and detect internal scatter due to water inclusions in temperate ice. The glaciological importance of this is twofold: bed topography is a primary component for modeling the long-term evolution of glaciers and ice sheets, and the presence of temperate ice and associated englacial water significantly reduces overall ice viscosity. Englacial water has a direct influence on radar velocity, which can result in incorrect observations of bed topography due to errors in depth conversion. Assessment of radar velocities often requires multi-offset surveys, yet these are logistically challenging and time consuming to acquire, hence techniques to extract velocity from common-offset data are required. We calculate englacial radar velocity from common offset GPR data collected on Von Postbreen, a polythermal glacier in Svalbard. We first separate and enhance the diffracted wavefield by systematically assessing data coherence. We then use the focusing metric of negative entropy to deduce a migration velocity field and produce a velocity model which varies spatially across the glacier. We show that this velocity field successfully differentiates between areas of cold and temperate ice and can detect lateral variations in radar velocity close to the glacier bed. This velocity field results in consistently lower ice depths relative to those derived from a commonly assumed constant velocity, with an average difference of 4.9 ± 2.5% of local ice depth. This indicates that diffraction focusing and velocity estimation are crucial in retrieving correct bed topography in the presence of temperate ice.

Plain Language Summary The internal structure and thickness of glaciers can often be mapped using a technique called ground-penetrating radar (GPR). To do this, we emit pulses of radio waves into the ice from the surface, and record the returning energy reflected back to the surface. Reflections are a result of contrasts in the material properties within the ice or at the ice-bed interface. Sometimes, glacier ice can have quantities of water stored within pores between the ice crystals; this complicates the mapping process as it scatters the radio signal, and distorts the image of the bed below by changing the speed at which radio waves travel through ice. In this paper, we apply a new technique to use this scatter to estimate the changes in radio wave velocity. We use this newly estimated radio wave velocity to improve our understanding of the shape of the bed, and to improve our understanding of water distribution within the glacier.

Key Points:

- We use diffractions in ground-penetrating radar data to retrieve the radar velocity field of a polythermal glacier
- The retrieved radar velocity field successfully differentiates between cold and temperate ice
- We use the retrieved velocity field to improve bed topography relative to a constant velocity field

Correspondence to:

R. Delf and R. G. Bingham,
r.delf@ed.ac.uk;
r.bingham@ed.ac.uk

Citation:

Delf, R., Bingham, R. G., Curtis, A., Singh, S., Giannopoulos, A., Schwarz, B., & Borstad, C. P. (2022). Reanalysis of polythermal glacier thermal structure using radar diffraction focusing. *Journal of Geophysical Research: Earth Surface*, *127*, e2021JF006382. https://doi.org/10.1029/2021JF006382

Received 30 JUL 2021
Accepted 12 JAN 2022

Author Contributions:

Conceptualization: Richard Delf, Robert G. Bingham
Data curation: Richard Delf, Robert G. Bingham, Chris P. Borstad
Formal analysis: Richard Delf
Methodology: Satyan Singh, Benjamin Schwarz
Software: Benjamin Schwarz
Supervision: Robert G. Bingham, Andrew Curtis, Antonios Giannopoulos
Visualization: Richard Delf
Writing – original draft: Richard Delf
Writing – review & editing: Richard Delf, Robert G. Bingham, Andrew Curtis, Satyan Singh, Antonios Giannopoulos, Benjamin Schwarz

1. Introduction

In this paper, we apply common-offset velocity analysis to conventional glaciological ground-penetrating radar (GPR) data acquired across an Arctic polythermal glacier. Our motivation is to improve constraints on the englacial temperate-cold ice distribution, and to improve the accuracy of survey-derived basal topography, which is often degraded beneath polythermal ice masses. The importance of this approach is twofold. The englacial radar velocity field is strongly indicative of the presence of interstitial water within ice (Benjumea et al., 2003; Björnsson et al., 1996; Bradford et al., 2009; Brown et al., 2017; Copland & Sharp, 2001; Murray et al., 2007) and hence constraining glacier-wide variations in radar velocity leads to a more complete understanding of the water content and temperate ice distribution within the glacier. Additionally, the application of GPR processing strategies to retrieve correct bed depth and topography is dependent on an accurate radar velocity field, yet this is often overlooked or poorly understood in studies quantifying ice volume or mapping bed topography of polythermal and temperate glaciers (Lapazaran et al., 2016).

Several approaches have previously been used to investigate the englacial radar velocity distribution of polythermal ice, including multi-offset (Bradford et al., 2009; Brown et al., 2017; Murray et al., 2007), common-offset (Benjumea et al., 2003; Bradford, 2005; Forte et al., 2014; Moore et al., 1999; Navarro et al., 2005), and down-borehole survey data (Gusmeroli et al., 2010). Common-offset data have also enabled direct estimation of englacial water content through radar backscatter amplitudes, yet these do not resolve velocity structure (Bamber, 1987; Hamran et al., 1996; Pettersson et al., 2004). Multi-offset approaches to velocity analysis rely on logistically challenging acquisition geometries to achieve suitable velocity precision (Barrett et al., 2007; Murray et al., 2007) and consequently do not presently offer a viable solution for most field acquisitions. Extracting an englacial velocity field from common-offset data has required users either to fit diffraction hyperbolae manually along the radar profiles (Benjumea et al., 2003; Moore et al., 1999; Navarro et al., 2005) or to retrieve the focusing velocity from migration velocity analysis (MVA) of diffractions (Bradford, 2005). While the MVA approach is time-consuming due to the manual nature of velocity picking, Bradford (2005) represents the most promising approach to date in generating a radioglaciological 2D velocity field for subsequent processing and interpretation, and the generated velocity model is subsequently used to estimate water content across a single GPR profile of Bench Glacier, Alaska. Automating this MVA approach to estimate water content over glacier- and ice-sheet scales is a principal motivation for the current study.

Here, we present a method for the automated estimation of a 2D englacial radar velocity field to provide an improved understanding of the temperate-ice distribution within a polythermal glacier using a series of 2D, common offset GPR data sets. The underpinning method of inverting from diffractions in common-offset data has been developed in seismic applications (Fomel et al., 2007; Preine et al., 2020; Schwarz & Gajewski, 2017), yet has previously been applied only manually to radioglaciological data (Bradford, 2005). We apply the workflow described here to field data collected on a polythermal glacier in Svalbard, and detect areas of low radar-wave velocity coincident with high signal scattering within the data, in accordance with previous studies on similar polythermal glaciers (Murray et al., 2007). We then use the resultant radar-wave velocity field to estimate the improvements in glacier bed topography, compared to the assumption of a constant representative ice velocity (Navarro et al., 2014).

2. Field Data and Acquisition

2.1. Physical Setting

Von Postbreen (78°25.07 N and 17°43.27 E) is a polythermal glacier (Sevestre et al., 2015) located in the Tempelfjorden region of Svalbard. It is approximately 15 km in length and has an area of 168 km^2 (König et al., 2014). The upper tributaries include Fimbulisen to the south, Potpeschniggbreen to the North-East, and Phillippbreen to the north. The lower ablation area consists of two tongues, the southernmost of which is the widest at 2 km width on average and forms the focus of this study. The glacier is classed as surge-type and is currently in a long quiescent phase, typical of many Svalbard glaciers (J. A. Dowdeswell et al., 1991), having last surged in 1870 (De Geer, 1910). Crevasse-squeezed ridges are present in the modern-day forefield and are noted as a sign of historic surging (Farnsworth et al., 2016). The glacier was historically confluent with Tunabreen with a continuous calving front in Tempelfjorden, but has steadily retreated throughout the twentieth century and is now entirely land-terminating (Flink et al., 2015; Sweeting & Groom, 1956). While Von Postbreen has been long quiescent, neighboring Tunabreen has surged regularly and is well-studied (How et al., 2019). The confluent minor glacier Bogebreen surged in 1980 (J. Dowdeswell et al., 1984).

Geophysical surveys on Von Postbreen were first undertaken in 1980 using an airborne radio echo sounding system with a central frequency of 60 MHz (Drewry et al., 1980), sounding both the bed and internal scatter within the ice as part of extensive surveys over the archipelago (J. Dowdeswell et al., 1984). Bamber (1987) applied a reflection coefficient-based analysis of the uppermost internal scattering horizon on similar glaciers across Svalbard from the same surveys, and concluded that it represents a layer of temperate ice with a water content of approximately 3%. In 2012 and 2015, Sevestre et al. (2015) undertook an extensive GPR campaign at 100 MHz, successfully mapping the distribution of temperate ice within the glacier, but encountering strong scattering throughout the deepest ice, precluding the ability to pick the bed confidently throughout.

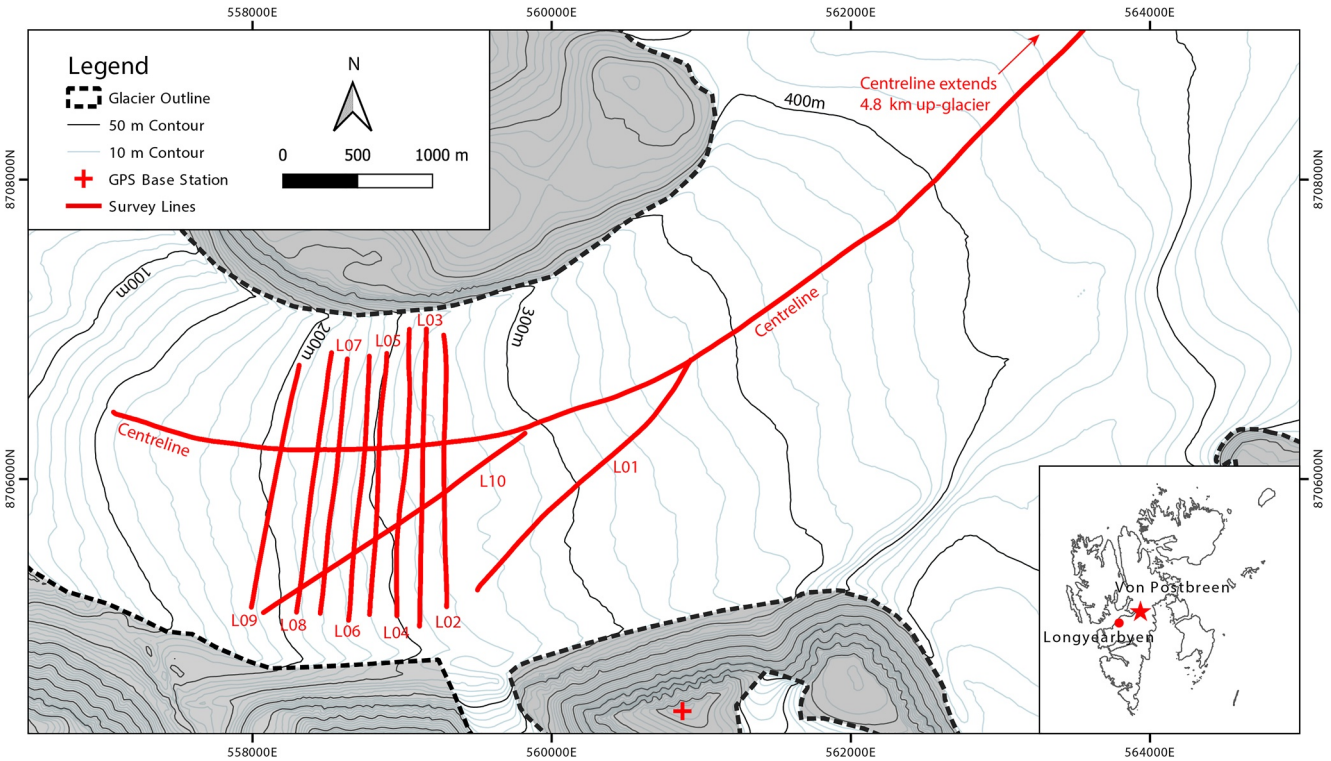

Figure 1. Map of Ground-Penetrating Radar lines collected in 2018 on the lower region of Von Postbreen, with location within Svalbard (inset). Tempelfjorden is to the west of the glacier front. The GPS base station was situated to the south of the glacier on Przybyllokfjellet. Contours are derived from Norwegian Polar Institute S0 DEM (Norwegian Polar Institute, 2014).

2.2. Data Acquisition

Data were collected on the 13 and 15 March 2018, using a 25 MHz PulseEkko Pro GPR system mounted on plastic pulks towed behind a snowmobile. We acquired eight transverse profiles across the ablation zone, each approximately 2 km long and spaced by 200 m, and a 13 km longitudinal profile extending to the upper accumulation zone (Figure 1). Antennas were mounted in a parallel endfire configuration in line with the direction of travel; antenna dipole centers were separated by an offset of 5 m, which in this study we refer to as a common-offset acquisition. A 4 ns sample interval (sampling frequency 250 MHz) was used which gives a good reconstruction of the received waveform, and a trace length of 1,125 samples was used. The snowmobile was driven at 10–15 km/hr, giving an average trace spacing in the raw data of 0.5 m. Traces were located with a Leica GS10 differential GPS rover feeding real time kinematic corrections directly to the GPR system, the base station for which was located on Przybyllokfjellet to the south of the glacier at an elevation of 720 m above sea level. The base station location was corrected using the Canadian Spatial Reference System Precise Point Positioning service following a 30 min static recording time on a previous day.

3. Methodology

The approach can be described in five main steps. We first pre-process the acquired radar data to remove significant noise sources. We then apply a diffraction enhancement algorithm to remove planar signals and noise in the data, and generate coherent diffractions. Then, following an approach previously developed and applied by Fomel et al. (2007) to assess the velocity from a post-stack seismic data set, we apply diffraction focusing to the radar profiles to generate time-domain englacial radar-wave velocity fields. We modify this approach by applying a novel focusing measure of the local signal entropy as a function of focusing velocity. We then undertake parameter testing on shaping regularization of the radar-wave-velocity field to assess the tradeoff between overfitting, with associated non-physical local velocities, and oversmoothing, whereby local anomalies are lost. Finally, we

use the estimated velocity field to (a) derive a model of water content distribution across the glacier, and (b) migrate and depth-convert the radar data to derive a correct bed topography model.

3.1. Pre-Processing

Data pre-processing was required before application of the velocity analysis algorithm. Traces were re-sorted to 1 m intervals using associated GPS locations. A static time shift was applied such that $t = 0$ ns at the first break of the direct arrival, followed by a 2 MHz high-pass (*dewow*) filter to remove low frequency or static, DC noise.

Due to the small offset between transmitter and receiver, imposed by logistical constraints, significant ringing noise was experienced through approximately the first 300 ns of each trace. To remove this noise, we used a modification of the singular value decomposition (SVD) filter, developed by Freire and Ulrych (1988) for seismic data and applied to helicopter-borne radar data over Glacier de la Plaine Morte, Switzerland, by Grab et al. (2018). This approach decomposes the radargram $\mathbf{D}$ of m traces and n data points to

$$\mathbf{D} = \mathbf{U}\mathbf{S}\mathbf{V}^T = \sum_{i=1}^{m} \sigma_i \mathbf{u}_i \mathbf{v}_i^T \tag{1}$$

where $\mathbf{U}$ is a $m \times m$ orthogonal matrix consisting of the eigenvectors $\mathbf{u}_i$ of the covariance matrix of $\mathbf{D}\mathbf{D}^T$, (the *left* singular vectors), $\mathbf{S}$ is a diagonal matrix whose diagonal elements are the singular values σ_i of $\mathbf{D}$ in descending order, and $\mathbf{V}$ is a $n \times n$ matrix of the eigenvectors $\mathbf{v}_i$ of $\mathbf{D}^T\mathbf{D}$ (the *right* singular vectors). Equation 1 shows that $\mathbf{D}$ can be reconstructed by a σ_i-weighted summation of the orthogonal eigenimages $\mathbf{u}_i\mathbf{v}_i^T$. The ringing noise constitutes a highly correlated signal between traces which can be described well by a low number of high-amplitude eigenvalues σ_i. Filtering is applied over $\mathbf{S}$, scaling high-amplitude values of σ_i and retaining low values of σ_i which constitute the uncorrelated internal reflections. To generate a modified vector $\hat{\mathbf{S}}$, and the filtered radargram is reconstructed by

$$\mathbf{D}_{\text{filt}} = \mathbf{U}\hat{\mathbf{S}}\mathbf{V}^T \tag{2}$$

This approach is successful in removing near-surface ringing, yet in the case of a flat or low-dip bed reflection, it can result in an additional attenuation of the bed reflection amplitude. We therefore modify this approach by applying a smooth amplitude taper to the data between $t = 0$ ns and a user-defined two-way travel time (twtt), such that we generate two matrices $\mathbf{D} = \mathbf{D}_{\mathbf{ns}} + \mathbf{D}_{\mathbf{bed}}$, where $\mathbf{D}_{\mathbf{ns}}$ captures the near-surface and upper scattering layer and $\mathbf{D}_{\mathbf{bed}}$ represents the deeper radargram including the bed, with data partitioned in twtt by a tapered transition. SVD filtering (Equations 1 and 2) is applied to $\mathbf{D}_{\mathbf{ns}}$, and the output radargram is reconstructed by $\mathbf{D}_{\mathbf{out}} = \mathbf{D}_{\mathbf{ns}_{\mathbf{filt}}} + \mathbf{D}_{\mathbf{bed}}$. Parameter testing is required on the scale of the pre-filter data partition (separating $\mathbf{D}_{\mathbf{ns}}$ and $\mathbf{D}_{\mathbf{bed}}$) which we generally define as a 100-sample plateau with a 200-sample cosine taper, and the filter of eigenvalues, which we scale from zero using a cosine taper over the first 20 values.

3.2. Retrieving the Diffracted Wavefield

Estimation of a full-ice-depth velocity field requires retrieval and focusing of diffractions throughout the ice column. The bed reflection is high-amplitude and specular in nature relative to diffractions within the ice. As such, there is little change with migration velocity perturbation, hence little variation in a time-velocity-domain common image gather. Suppression of the bed reflection is therefore essential to see the diffracted signals clearly, and thus enable retrieval of a full-depth average velocity and interval velocity of the deepest regions of ice.

We use a coherent summation and subtraction scheme (Schwarz, 2019) to extract diffraction-only data from the pre-processed radar lines. This is a three-step process: first, the slope of arriving wavefronts is estimated by a directional stacking optimization problem; second, planar wavefronts are subtracted from the raw data; and third, the diffractions are further enhanced by applying local time and amplitude corrections.

To remove planar wavefronts, the coherence of arriving wavefronts is estimated as a directional stacking optimization problem. For every data point $\mathbf{D}(x_0, t_0)$, an estimation of the inclination of the most coherent arrival can be represented as an optimization problem using the semblance norm (Neidell & Taner, 1971), in which the horizontal slowness p acts as the optimization parameter

$$\max_{p} \frac{1}{n} \frac{\sum_{\delta t} \left(\sum_{i=1}^{n} \mathbf{D}[x_0 + \Delta x_i, t_0 + 2p\Delta x_i] \right)^2}{\sum_{\delta t} \sum_{i=1}^{n} \mathbf{D}^2[x_0 + \Delta x_i, t_0 + 2p\Delta x_i]}, \tag{3}$$

where the index i refers to the ith trace within a spatial aperture, and δt is a time window over which summation is performed.

To ensure reliable convergence even in the case of strong interference and noise contamination, the problem expressed in Equation 3 is solved within a local aperture spanning n traces using a global differential evolution optimizer that is constrained to low wavenumbers (Storn & Price, 1997). Directional stacking on the original data is then applied using the resultant slope field, leaving strong, near-planar reflections which are subtracted from the raw data to leave high slope angle arrivals (Schwarz & Gajewski, 2017). Used alone, this step provides an approximately diffraction-only data set, yet much of the high-frequency scatter is retained in temperate ice, resulting in imperfect and noisy hyperbolas. In addition, the derived low-wavenumber wavefield may encode sufficiently accurate waveforms, but is likely to suffer from amplitude deviations and temporal offsets, which can compromise the subsequent step of noise attenuation.

To enhance the diffracted wavefield further and suppress high-frequency scatter, we follow Schwarz (2019) in applying a least squares optimization approach to subtract the previously obtained low-wavenumber estimate from the input data. The optimization for the local amplitude scaling α_0 and a local time shift τ_0 minimizes the misfit

$$\min_{\alpha_0, \tau_0} \sum_{\delta t} \sum_{i} \left[\mathbf{D}(x_i, t_i) - \alpha_0 \mathbf{D}_{low}(x_i, t_i + \tau_0) \right]^2 \tag{4}$$

where $\mathbf{D}_{\text{low}}$ is the coherent reflection model estimated in the previous step. To remove planar wavefronts and estimate the local slope, we used an aperture of 20 m, a coherence window of 20 ns and a maximum angle of incidence of 3°. Diffraction separation and coherent stacking were then performed with a wider aperture of 100 m, with a temporal adaptation window of 100 ns (δt in Equation 4). The result can be considered to be a diffraction-only data set with contaminating noise and planar reflections suppressed. We apply this approach to our data, and use this diffraction-only data set going forward for velocity analysis.

3.3. Time Migration Velocity Analysis

We follow the approach of Fomel (2003) to estimate time-migration velocity field using local focusing velocities for each hyperbola in the data set. This step, and subsequent processing, are undertaken in Madagascar, an open-source geophysical processing package (Madagascar, 2021). An initial Stolt F-K migration is applied using a velocity of 0.1 m/ns, which is below the minimum expected value for radio-wave transit through glacier ice. We then apply velocity continuation using a velocity interval of 0.005 m/ns up to 0.2 m/ns to produce a 3D data volume $\mathbf{D}(t, x, v)$. To constrain the focusing function, we chose a velocity discretization of 0.005 m/ns as a balance between velocity precision and computational demand; this follows the discretization used in the manual MVA approach of Bradford (2005).

We measure the level of local focusing through use of the statistical measure of negative entropy. First introduced by Shannon (1948) as a measure of information order in communications technology, the concept of negative entropy as a measure of signal focusing was extended and subsequently applied to diffraction imaging by De Vries and Berkhout (1984) by calculating the measure of focusing for a constant-velocity migrated data set to estimate a constant migration velocity for the whole data set. The concept can be extended to a 2D $v(x, z)$ problem through the use of moving windows. This can be achieved by first applying a Hilbert transform to generate amplitude data a_{ij} of amplitude a at pixel i, j, and calculating negative entropy focusing (S) by

$$S = \frac{1}{N} \sum_{i=1}^{N1} \sum_{j=1}^{N2} (a'_{ij}) \log(a'_{ij}) \tag{5}$$

for each location throughout the data, where

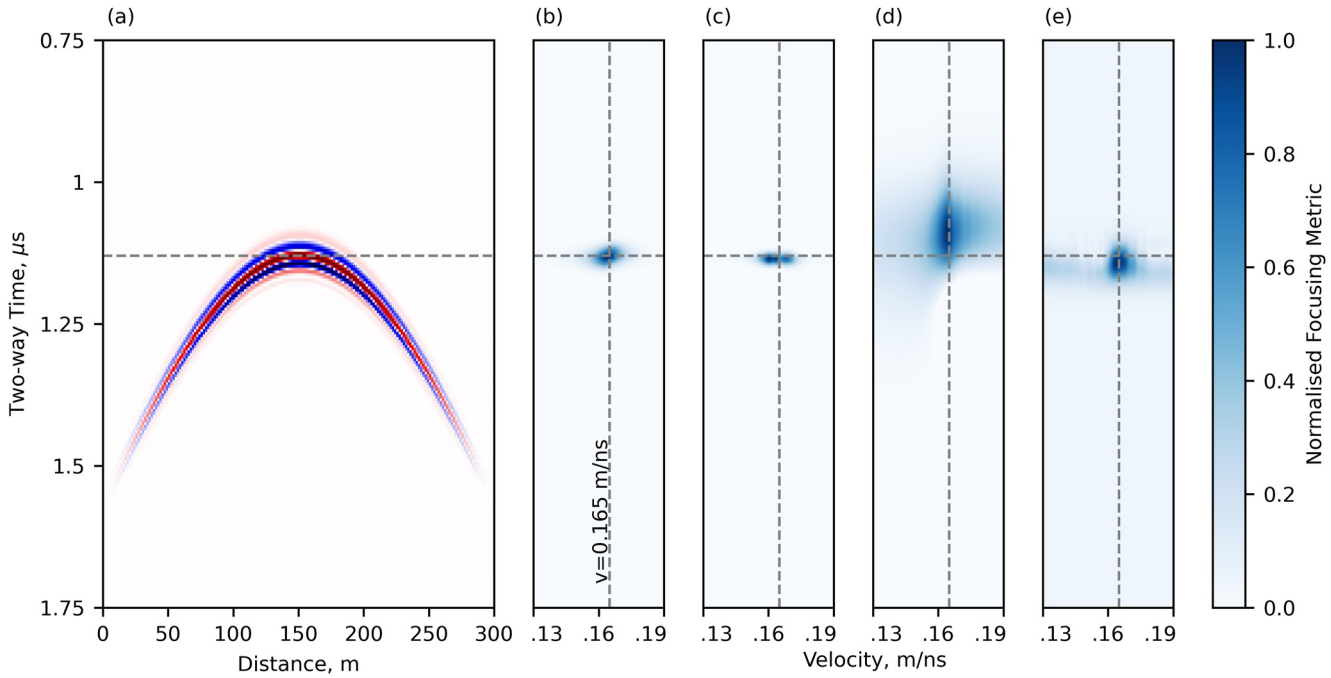

Figure 2. Comparison of focusing functions on a semblance-like time-velocity panel for a synthetic single diffraction (a). Panels are extracted for the center point of the diffraction and normalized. (b) Negative entropy calculated as a continuous function. (c) Negative entropy calculated using moving windows. (d) Semblance and (e) Kurtosis, as used in (Fomel, 2003).

$$a'_{ij} = \frac{a_{ij}}{\frac{\sum_{i,j} a_{ij}}{N}} \tag{6}$$

is the data amplitude normalized by the mean over an $N1 \times N2$ moving window, and $N = N_1 N_2$, the number of cells in the moving window. Each window is tapered with a Gaussian kernel such that only the central pixels of the window are equal to the input data. This approach using moving windows is highly computationally intensive, and we therefore calculate S using an alternate approach, by scaling all-positive amplitude data using a 2D automatic gain control (AGC) filter on which we calculate local negative entropy by

$$S = ag(x,t)\log(ag(x,t)) \tag{7}$$

where $g(x, t)$ is the AGC gain function (Yilmaz, 2001)

$$g(x,t) = \frac{1}{\sqrt{\frac{1}{N}\sum_{i=1}^{N} a_i^2}} \tag{8}$$

and a is the Hilbert-transform derived amplitude as previously. This results in one calculation to estimate $g(t)$ within a moving window, followed by a point-wise calculation of S (Equation 7), and is significantly more computationally efficient. The result is a statistical measure of the degree of signal focusing for each location within the data; this metric is calculated for each constant migration panel.

Figure 2 compares the performance of negative entropy to the continuous and windowed negative entropy function, semblance, and kurtosis measures of focusing. The diffraction is modeled at a depth of 100 m within a homogeneous medium of $v = 0.165$ m/ns, representing an anomaly within a cold ice medium. The diffraction is focused using a velocity range of 0.13–0.19 m/ns. We find that the negative entropy measure gives an improved metric of focusing. This is principally because negative entropy is less susceptible to the presence of multiple wavelet cycles typical of GPR data, as discussed by Booth et al. (2010), in addition to being less sensitive to regions of noise and crossing diffraction tails in the data. This is beneficial in the application of automated picking algorithms as in the subsequent step, where the focusing metric is used as an objective function to maximize

(Toldi, 1989), as it avoids the potential of small-scale local maxima which may lead to an incorrect velocity pick in the case of semblance or kurtosis (Figures 2c and 2d).

Automated velocity picking from focusing image gather panels is undertaken by maximizing the function (Fomel, 2003; Toldi, 1989).

$$P[v(t)] = \int_{t_{\min}}^{t_{\max}} S(t, v(t))dt, \tag{9}$$

In practical terms, this seeks to find a surface in the trace-twtt axis through the 3D focusing volume generated in the previous step, which maximizes the sum of focusing across the surface. This generates a surface which is constrained by peaks in the focusing metric and enables a controlled interpolation between. The picking algorithm is undertaken in a two-step process. The first step maximizes the function in Equation 9 for each trace to give a coarse, strongly laterally variant velocity field. The maximum vertical gradient of the picked velocity profile is dictated by defining the picking gate, that is, the maximum variation in velocity between time samples, and a starting velocity is provided giving the surface velocity. In the absence of near-surface diffractions we estimate this velocity the velocity of radar through cold ice with a small air fraction, the calculation for which is discussed in Section 3.5. A second step undertakes smoothing through shaping regularization in trace and time coordinates (Fomel et al., 2007), to limit the gradient. We then apply a time backshift $\Delta t = 5.6 \times 10^{-9} s$ to the data, to account for the time difference between the wavelet maximum and first break (Booth et al., 2010). The derived velocity field is considered to be an average between the surface and the scattering point, which we henceforth refer to as V_{RMS}. A smooth Dix inversion (Dix, 1955; Fomel, 2007), is then applied to V_{RMS} to derive the local velocity, which we refer to as interval velocity or V_{local}.

3.4. Migration and Depth Conversion

With the assumption of a constant velocity field, Stolt (Hambrey et al., 2005; Murray et al., 1997; Navarro et al., 2014; Saintenoy et al., 2013) or Kirchhoff migrations (Arcone et al., 1995; Schannwell et al., 2014; Sevestre et al., 2015) have been commonly applied to similar glacier GPR surveys on polythermal glaciers. In exploration seismic imaging, depth migration or reverse time migration (RTM) is undertaken when there are lateral variations in interval velocity due to the effect of energy refraction with depth (Yilmaz, 2001). Some studies have used RTM with airborne GPR data over temperate ice to reconstruct bed topography, where two constant velocity layers are required due to the elevated platform (Grab et al., 2018; Langhammer et al., 2019), yet this approach is not widely implemented due to the wavelength and model scales required. Assuming a migration aperture of 200 m, while we expect a degree of lateral variation in the velocity field, the magnitude and scale of velocity variations is minimal on the scale of the migration algorithm aperture as a result of the regularization used in the velocity picking step. For this reason, we apply Kirchhoff time migration followed by a 1D, trace-by-trace depth conversion, both using the derived V_{RMS} model.

3.5. Water Content Inversion

Inversion for water content requires the assumption of a geophysical mixing model. Previous studies have used the Looyenga mixing model (Macheret et al., 1993; Murray et al., 2007), which makes the assumption of isotropic and spherical inclusions in a two-phase mixture, or the Complex Refractive Index Model (CRIM; Bradford et al., 2009; Brown et al., 2017) which allows inclusion of an arbitrary number of phase contributions by estimating a time-averaged slowness weighted using the relative volumetric contributions of each phase (Greaves et al., 1996). More advanced mixing models include the formulation of Giordano (2005), which considers the case where water is held within disc-shaped inclusions with a preferred orientation resulting in an anisotropy in velocity. This was used by Bradford et al. (2013) to quantify anisotropy on Bench Glacier, Alaska. Analysis of the bed pick at survey line intersections in our data collected on Von Postbreen shows most intersections are within a 50 ns (≈4 m at 0.166 mns^{-1}) time difference, showing little evidence of significant anisotropy, hence we use the CRIM equation.

We treat the glacier as a three-phase material whereby pore spaces are made up of water or air pockets, and as such the water content by volume can be estimated by

$$\phi_w = \frac{\frac{1}{v} - \frac{1}{v_i} - \phi_a\left(\frac{1}{v_a} - \frac{1}{v_i}\right)}{\frac{1}{v_w} - \frac{1}{v_i}} \tag{10}$$

where ϕ_w and ϕ_a are the volumetric water and air fraction, respectively, v is the estimated local velocity, and v_i, v_w, and v_a are the velocity of propagation through ice, water, and air.

The fraction of air in glacier ice, held within pockets and bubbles, decreases as a function of depth due to closure as a result of overburden pressure (Cuffey & Paterson, 2010), and must be estimated for Equation 10 to remove a possible depth-dependent bias in water content. Using the assumption of zero deviatoric stress, Bradford et al. (2009) balance the gas pressure within bubbles with the hydrostatic pressure due to an ice overburden to show that the volumetric air fraction ϕ_a as a function of depth z, calculated at a depth discretized by Δz, is

$$\phi_{a(n+1)} = \frac{KT_0}{\left[g\rho\Delta z \sum_{k=1}^{n}(1-\phi_{a(k)})\right] + P_0} - K\beta' \tag{11}$$

where g is acceleration due to gravity (9.81 ms^{-2}), ρ the density of ice (918 kg/m^3) and $K = \phi_0 R/M$, the volumetric contribution of air in ice at the surface scaled by R, the ideal gas constant and M, the molar volume of air at atmospheric pressure. $\beta' = 9.8 \times 10^{-8}$ K Pa^{-1} is a constant representing the rate of change of melting point with pressure, and P_0 is the atmospheric pressure at the surface. $\phi_{a(0)}$ is the air fraction at the surface, which is assumed to be 0.1.

3.6. Uncertainty Analysis

Uncertainty in water content can be estimated with propagation of errors using partial derivatives (Bradford et al., 2009). We consider contributions from uncertainty in air fraction σ_a, uncertainty in Dix-inverted interval velocity σ_v, and uncertainty in cold ice velocity σ_{v_i}. σ_a and σ_v are estimated through partial differentiation of the CRIM equation (Equation 10);

$$\sigma_v = \delta\phi_{w,v} = \frac{\frac{\delta v}{v^2}}{\frac{1}{v_i} - \frac{1}{v_w}} \tag{12}$$

$$\sigma_a = \delta\phi_{w,\phi_a} = \frac{\delta\phi_a\left(\frac{1}{v_a} - \frac{1}{v_i}\right)}{\frac{1}{vi} - \frac{1}{v_w}} \tag{13}$$

and

$$\sigma_{v_i} = \delta\phi_{w,v_i} = \frac{\delta v_i(\phi - 1)}{v_w\left(\frac{v_i}{v_w} - 1\right)^2} \tag{14}$$

and the total error, assuming the error in v and error in ϕ_a are uncorrelated, is

$$\sigma_w = \sqrt{\sigma_v^2 + \sigma_a^2 + \sigma_{v_i}^2} \tag{15}$$

The uncertainties in the radar velocity in water v_w and in air v_a are negligible, as these materials have well-defined real dielectric constants of 81 and 1 (Daniels, 2004), respectively, hence their contribution to uncertainty can be ignored for this analysis. The velocity of cold ice v_i is estimated using the derived velocity above the scattering region and below 50 m depth (i.e., in cold ice and where $\phi_a < 0.02$) and δ_{v_i} is estimated from the distribution of the derived velocity. Consistent with the uncertainty estimations of ϕ_a from Bradford et al. (2009), we hold the uncertainty in air fraction as $\delta_{\phi_a} = 0.5\phi_a$ which allows a significant variation in air fraction estimation given the simplified nature of ϕ_a estimation.

We now wish to estimate the uncertainty in local velocity, first considering the effects of the width of peaks in the negative entropy peaks in the velocity panels (as in Figure 2b), and second considering the influence of

propagating these uncertainties through the Dix velocity inversion step. The uncertainty in V_{RMS} is estimated by assessing the width at half maximum of the negative entropy peaks derived from Equation 7. The negative entropy response in Figure 2b shows a width at half maximum of ± 0.075 m/ns, which we use as an uncertainty going forward. Note that, as this is an uncertainty in V_{RMS}, this can be used directly as an estimate of the uncertainty in bed topography correction. To estimate the uncertainty in interval velocity we must consider the implications of propagating this error in V_{RMS} through a smooth Dix inversion algorithm. To do so, we use a Monte Carlo approach to velocity analysis using an example trace, similar to Booth et al. (2011), but using a continuous function of V_{RMS}. We generate an ensemble of 100,000 traces with added random Gaussian noise with a standard deviation $\sigma = 0.075$ mns^{-1}, matching that of the V_{RMS} range estimated above, smoothed over a scale factor of 10 pixels. We then undertake Dix inversion on all 100,000 noisy V_{RMS} trajectories independently and calculate a 1D depth-dependent estimate of ensemble standard deviation. Due to the computational cost of this approach in 2D, we repeat this in 1D for a single trace and use the standard deviation in local velocity as representative for the wider data set; an alternative approach to uncertainty analysis with a lower computational cost would be desirable for operational use, however this approach is sufficient for this study.

3.7. Manual Validation of Velocity Field

We validate the results of velocity estimation by manually estimating the V_{RMS} for survey line 5, taken across the glacier. We use the approach of Booth and Pringle (2016) for calculating the semblance response of individual hyperbolas and picking the semblance response of the first peak of the wavelet. Uncertainties on velocity are estimated using the width of the semblance response at 50% of the semblance peak. We pick semblance peaks for clear hyperbolas at two depths within the ice: along the uppermost surface of the scattering layer, and at or immediately above the ice-bed interface. For picks close to bed, we pick hyperbolas with no high-amplitude features immediately above, which may indicate multiples from sub- or englacial channels (Stuart, 2003) and hence focus at a lower V_{RMS} than primary diffractions. We use the coherence-enhanced diffraction-only data set, as data with only pre-processing applied do not contain sufficient diffraction hyperbolas to enable this approach.

4. Results

4.1. Diffraction Focusing

We apply the preprocessing, SVD filtering, and coherent wavefield separation and stacking to each acquired survey line and present the results from a radargram taken across-glacier in Figure 3. Figures 3a and 3b show the significant near-surface ringing in the pre-processed data, which was effectively removed by SVD filtering (Figure 3c) without lateral smearing or degradation of near-surface hyperbolas ("A" in Figures 3b and 3d). The SVD approach additionally handled changes in the noise characteristics along the survey line well ("B" in Figures 3b and 3d), and was successful in preserving the bed reflection throughout.

Coherent wavefield separation and stacking enhanced diffractions at the bed while removing planar bed returns, enabling estimation of V_{RMS} for the full ice depth throughout much of the survey area. Figures 3e and 3f show the resultant diffracted wavefield. Coherent diffractions can be detected throughout the ice column within the scattering region (highlighted as "A" and "C" in Figures 3b, 3d, and 3f), and planar reflections have been removed. Some residual noise in the near-surface is additionally further suppressed in the diffraction-only data set.

4.2. Velocity Picking and Validation

Figure 4 shows three example negative entropy panels from a segment of line 05 across the glacier, showing the correspondence of negative entropy peaks to prominent diffractions throughout the data. As there are no diffractions to estimate a starting velocity in the upper sections of ice, we use a starting pick velocity of 0.173 mns^{-1}, estimated through using Equations 11 and 10 (estimating v with $\phi_w = 0$) to represent the velocity in the uppermost ice across the glacier. Note that due to smoothing across traces, the picked V_{RMS} profiles do not pass through all peaks in the panel but nevertheless provide a representative V_{RMS} across the regularization aperture.

We perform a sensitivity analysis on the picked and Dix-inverted velocity field to select regularization scales by testing the results of a range of distance and twtt smoothing windows, after Nicolson et al. (2014). Figure 5 shows the result of testing a range of regularization windows for a single cross-line data set. Small regularization radii

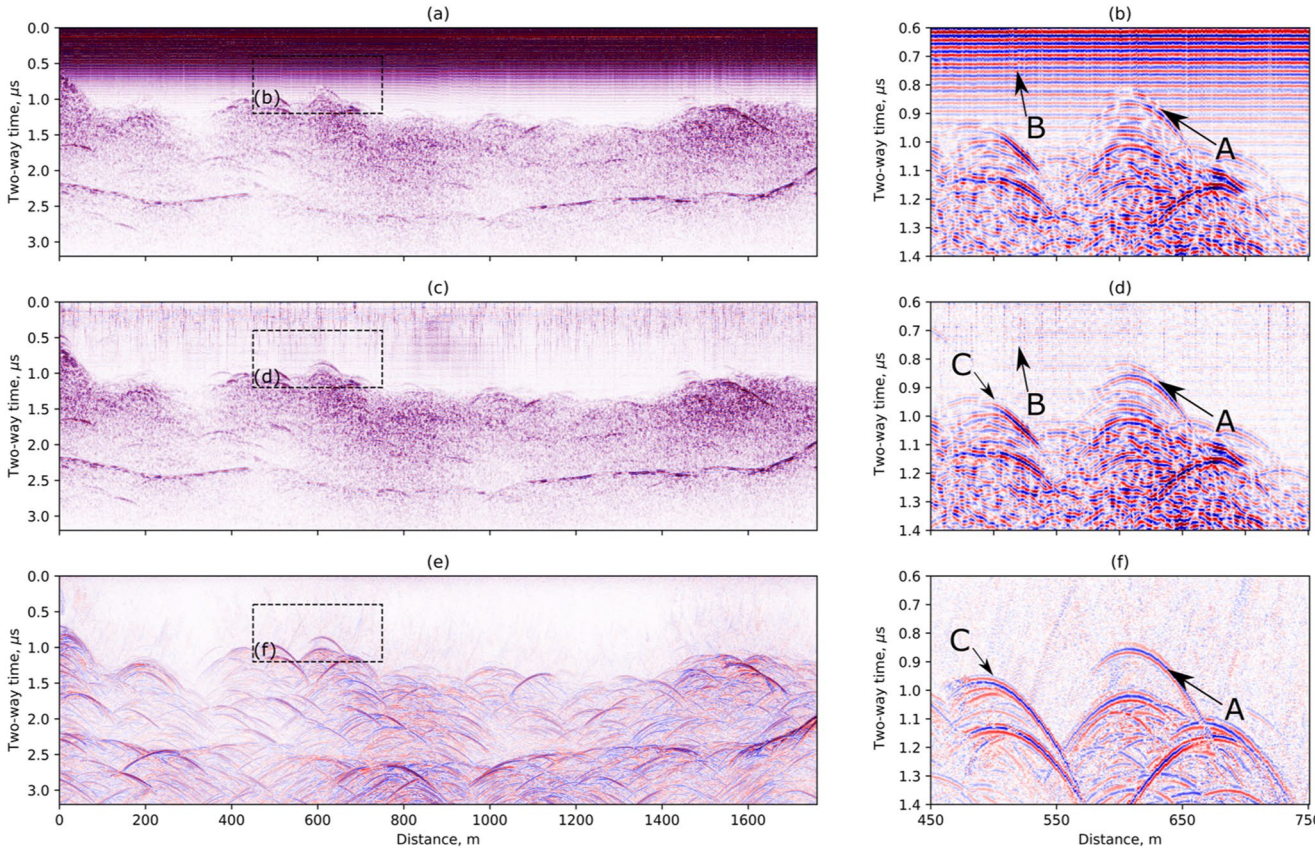

Figure 3. (a) Data from line 02 with only trace spacing corrections and *dewow* filter applied, showing significant ringing in the near surface (b) sub-set of data from the rectangle in panel (a). Panels (c and d) show data following singular value decomposition pre-processing, with much of the near surface ringing suppressed. Panels (e and f) show data after the coherence-based extraction of diffractions (Schwarz, 2019). Planar reflections are removed and the diffractions are enhanced ("A" and "C") and ringing is successfully removed through much of the profile ("B").

result in overfitting of Dix-inverted radar velocity (to the upper left of Figure 5). Cases with velocities below 0.1 and above 0.18 m/ns are rejected as these correspond to physically unreasonable velocities and are likely to be as a result of overfitting, and rapid transitions in average englacial water content are unlikely over short length scales. At large regularization scales, the velocity of the upper ice column reduces indicating an oversmoothing of low velocities into the higher-velocity upper layer, and a loss of distinctive cold/temperate ice distribution. In general, we find that a large smoothing radius is required to minimize rapid local transitions in velocity, which resulted in extreme local velocities. We used a window size of 100 m laterally and 50 samples in time (0.2 μs) across all lines for consistency, corresponding to panel (i) in Figure 5.

We manually pick the location of the apex of 13 diffractions across the top of the scattering layer and 11 diffractions at or immediately (<100 ns twtt) above the bed throughout the data. Figure 6 shows the extracted V_{RMS} from the bed pick compared to the manually derived velocities. The uncertainty in Figure 6 is the uncertainty in V_{RMS} as derived in Section 3.6. The manually derived picks do show some variations on short length scales which are not fully resolved by the automated approach (such as at 200 m in Figure 6b) but in general, the diffraction focusing-derived velocity field closely matches the manually derived picks to within the estimated uncertainty.

4.3. The Thermal Structure of Von Postbreen

Figure 6a presents an elevation-corrected radargram, produced assuming a constant englacial velocity field, along the full 13 km centerline profile through Von Postbreen. The profile excludes only the uppermost 900 m and lowermost 1.1 km of the glacier, where we could not gather data. On top of the radargram, we have superimposed a manually picked upper surface of the scattering zone, a surface that elsewhere has been taken as the interface between cold and warm ice (Bamber, 1987; Irvine-Fynn et al., 2011; Schannwell et al., 2014) and hence is hereafter

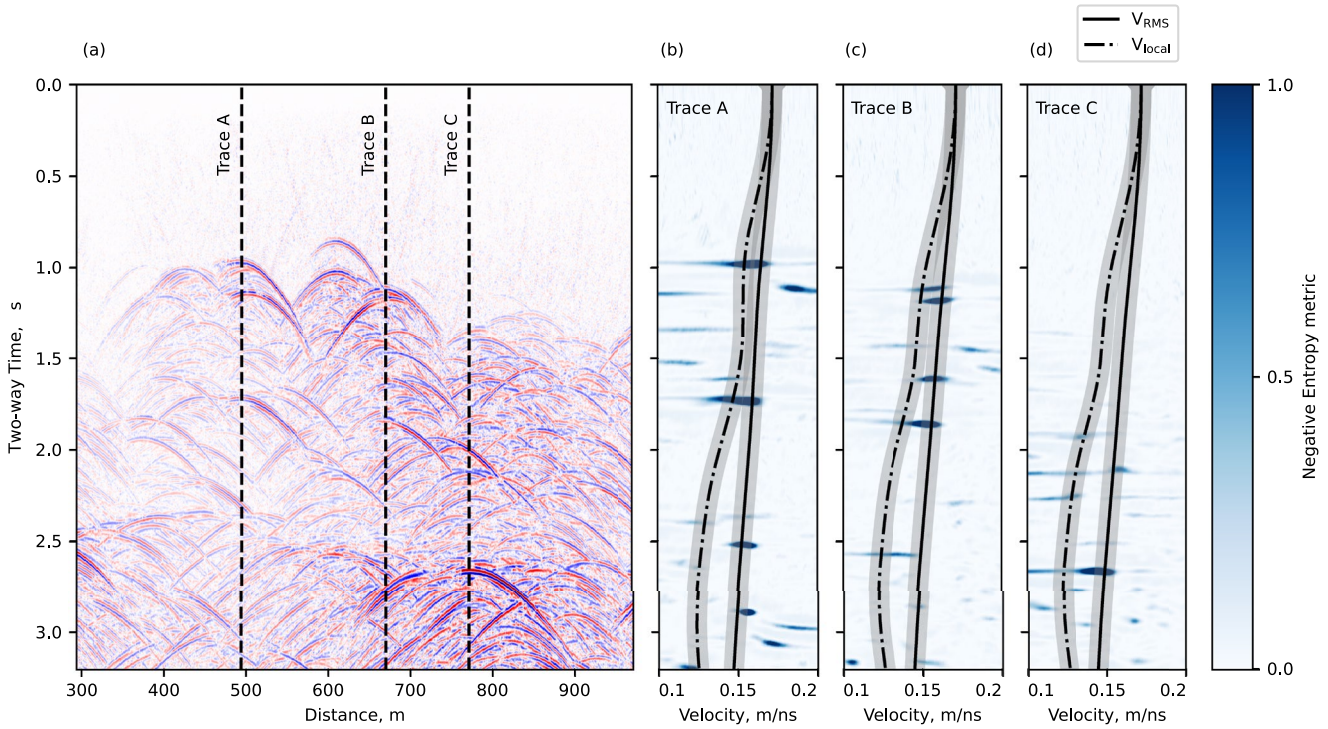

Figure 4. Application of the focusing function and automated picking algorithm to data. (a) Data from line 05 after pre-processing and coherent diffraction retrieval processing. Dashed lines in panel (a) show the location of the focusing images shown in panels (b, c, d). (b) Negative entropy metric estimated for the range of velocities 0.1–0.2 m/ns, extracted at trace A in panel (a). Panel (c) same as panel (b) for Trace B, and panel (d) same for Trace C. V_{RMS} (solid line) and V_{local} (dashed line) show the velocity profiles after picking and Dix velocity inversion, extracted for each trace are overlaid in panels (b, c, d). Gray areas around the velocity profiles shows uncertainty estimated in Section 3.6.

termed the cold/temperate-ice transition zone (CTZ). This shows that the glacier has a typical Svalbard- or Scandinavian-type thermal structure, whereby temperate ice makes up much of the ice column in the accumulation area and is advected downglacier to the ablation zone, where a layer of cold ice is present close to the surface across the ablation zone (Blatter & Hutter, 1991; Irvine-Fynn et al., 2011).

Data collected in the upper accumulation area depict scattering with an upper surface between 50 and 100 m below the surface across the upper 2 km of Von Postbreen. We are unable to determine if this extends to the surface as ringing in the near surface has resulted in data clipping, hence SVD filtering in pre-processing would be unable to retrieve this near-surface scatter. Such scattering is expected in the near surface however due to heterogeneities within the snow and firn layers in the accumulation zone, and was present in surveys undertaken by Sevestre et al. (2015). The lower ablation region consists of a layer of cold ice of approximately 80 m thickness overlying temperate ice in the lower ablation zone (up to 2 km in Figure 7). Our centerline does not capture the glacier front, which is approximately 1.1 km from the survey start point. Figure 7a shows the CTZ to be coincident with the bed at the survey start point, and it is likely therefore that the glacier is cold-based for the lowermost 1 km.

There is significant topography in the CTZ along the glacier centerline, with high-amplitude scattering reaching close to the surface at 2 and 5 km in Figure 7a. These are likely to correspond to crevasses or moulins whereby surface meltwater is able to access the englacial hydrological system during the summer melt, potentially enhancing local englacial melt. No clear surface features were apparent when undertaking the survey. Further topography is seen at approximately 10 km, where a small high in CTZ topography is seen up-glacier of a significant bed topography high.

The diffraction focusing-derived radar-wave interval velocity field (V_{local}) along the same profile (Figure 7b) resembles structurally the contrasts in scattering depicted by Figure 7a. The upper ice column is characterized by higher velocities, generally 0.16 m/ns, while the lower ice column consists of lower velocities, generally ranging between 0.14 and 0.15 m/ns. The distribution of velocities above and below the manually derived CTZ is shown in Figure 8, reflecting the ability of the approach to differentiate the radar-wave velocities in the respective

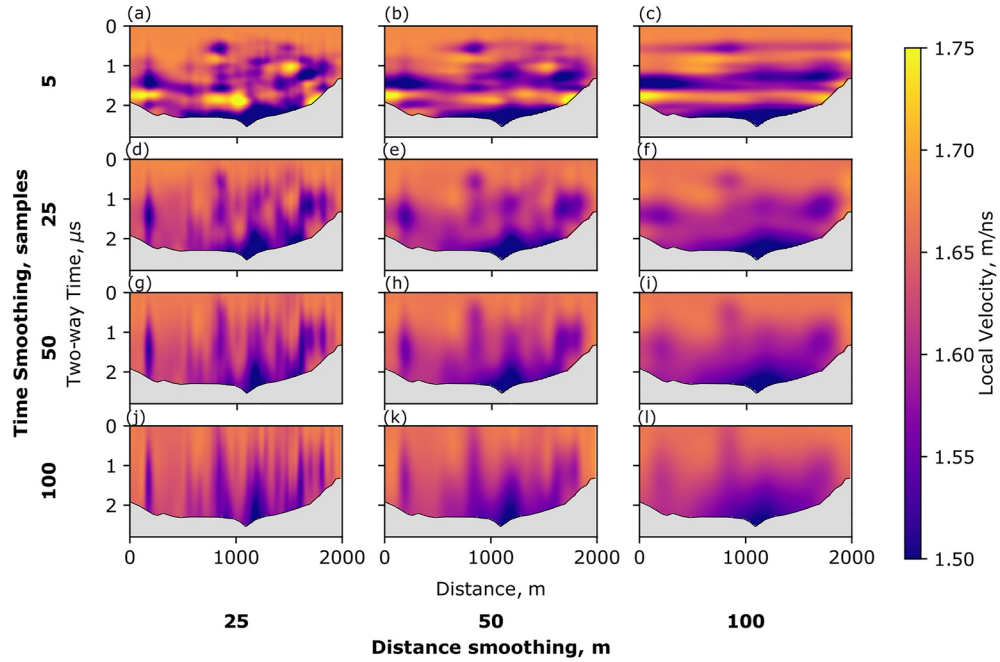

Figure 5. Testing picking regularization parameters using an example cross-line data set. Panels (a–c) show smoothing with the smallest (5-sample) window in the time-direction, with each subsequent row showing smoothing radii of 25, 50, and 100 samples. Panels (a, d, g, j) show smoothing with the smallest (25 m) window in the trace orientation (x-direction), with subsequent columns showing smoothing over 50 and 100 m smoothing. A low distance smoothing results in physically unreasonable velocity models with very rapid lateral changes in velocity. A low time smoothing parameter increases the chance of velocity spikes outside the expected range of 1.4–1.7 $\times$ 10^8 m/s after Dix velocity inversion. Data are clipped before the bed reflection to avoid fitting to subglacial diffractions.

thermal regimes. Several regions of very low velocity (down to 0.13 m/ns) are found in the lower glacier (at approximately 3.8 and 5.4 km). The mean velocity below the scattering interface is 0.150 $\pm$ 0.004 m/ns, with the mean above being 0.159 $\pm$ 0.006 m/ns, although with a significant negative skew with a peak at 0.165 m/ns. This peak corresponds well with typical values for cold ice of 0.165–0.168 m/ns (Bradford et al., 2009; Navarro et al., 2014).

Figure 7c shows the englacial water content distribution derived from Figure 7b. We estimate the uncertainty in englacial water content, following Equation 15, to be $\pm$1.6%. Some regions of cold ice within the upper ice column have non-zero water content estimated, which may be a reflection of this uncertainty.

4.4. Glacier Bed Topography Reconstruction

We compare the results of undertaking bed topography estimation using an assumed englacial velocity of 0.166 mns^{-1}, as used by Navarro et al. (2014) to our newly derived radar velocity. Figures 9a shows the glacier-wide retrieved bed depth using picked velocities. Figure 9b shows the difference between the bed topography of Figure 9a and bed topography retrieved using the constant velocity of 0.166 mns^{-1}. The histogram in Figure 10 shows the distribution of differences between bed topography reconstructions across the glacier. We observe that ice depths derived using the picked velocity are consistently lower, with an average difference of 4.9 $\pm$ 2.5%, equivalent to 12.0 $\pm$ 8.4 m between constant- and picked-velocity bed topography.

5. Discussion

5.1. The Velocity Structure of Von Postbreen

In Figure 7, we show the retrieved velocity structure with the interpretation of the upper scattering layer, which is representative of the interface between cold and temperate ice in a polythermal glacier. Figure 8 shows the distribution of local velocities below the interpreted CTZ. These both show significant variations in local velocity

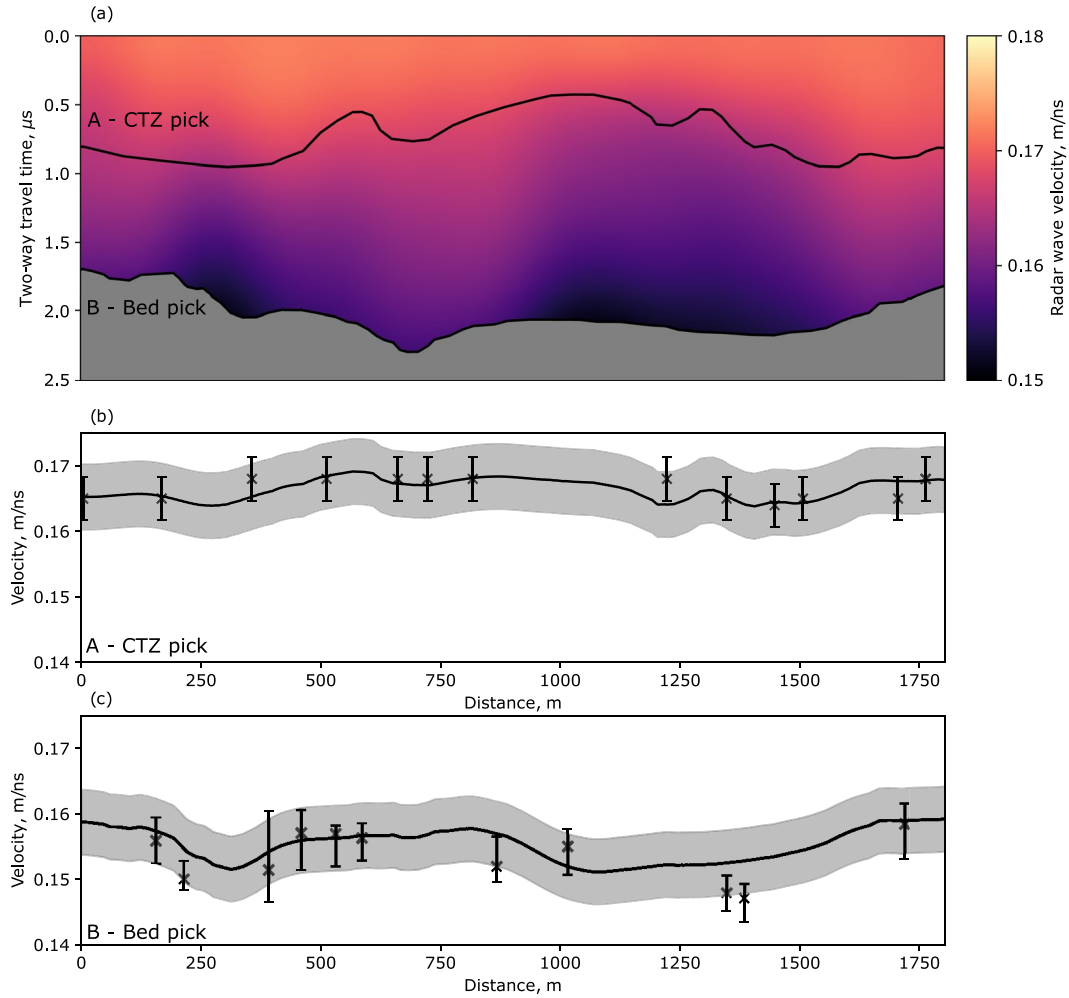

Figure 6. (a) V_{RMS} field for line 05 across the lower ablation zone of Von Postbreen. (b) The continuous line shows V_{RMS} extracted from the retrieved data in panel (a) for the cold-temperate ice transition zone (CTZ), with uncertainty in V_{RMS} in gray. Crosses show manually picked V_{RMS} from diffractions along the upper CTZ, with uncertainties estimated from the width at half maximum of the semblance response. Panel (c) same as panel (b), but using manually picked diffractions at or immediately above the bed.

below the CTZ along the length of the centerline profile, with a range of 0.131–0.164 mns^{-1}. This is representative of lateral variations in water content through the glacier. Of particular note are areas of very low velocity at or down-glacier of regions of enhanced scattering (approximately 2 and 5 km in Figure 7a), where the upper scattering layer extends into the upper ice column. Given the low prevalence of crevassing across much of the glacier surface, this is likely to be a small moulin whereby water is accessing the glacier interior over the summer melt season and either (a) being held within the ice as part of a disconnected englacial drainage system or (b) enhancing local melt through release of latent heat. Our data were collected in spring, before significant seasonal melt began, hence this enhanced englacial scatter is likely to have been persistent through winter and represent seasonal storage of water. Similar undulations in the upper surface of the scattering zone have been observed in the presence of surface crevassing and moulins at Hansbreen, Svalbard (Moore et al., 1999), and seasonal changes in the vertical distribution of water content have been observed, whereby a decreased scattering intensity at the CTZ may be attributed to enhanced drainage through the summer melt season (Jania et al., 2005). A similar conceptual model of overwinter englacial water storage is proposed by Irvine-Fynn et al. (2006) using repeat GPR surveys over the polythermal Stagnation glacier, Canada, suggesting that the englacial piezometric surface is elevated in the early melt season due to an inefficient englacial drainage system. This may be consistent with observations of Hodson et al. (2005), who hypothesize that over-winter subglacial storage of water is necessary

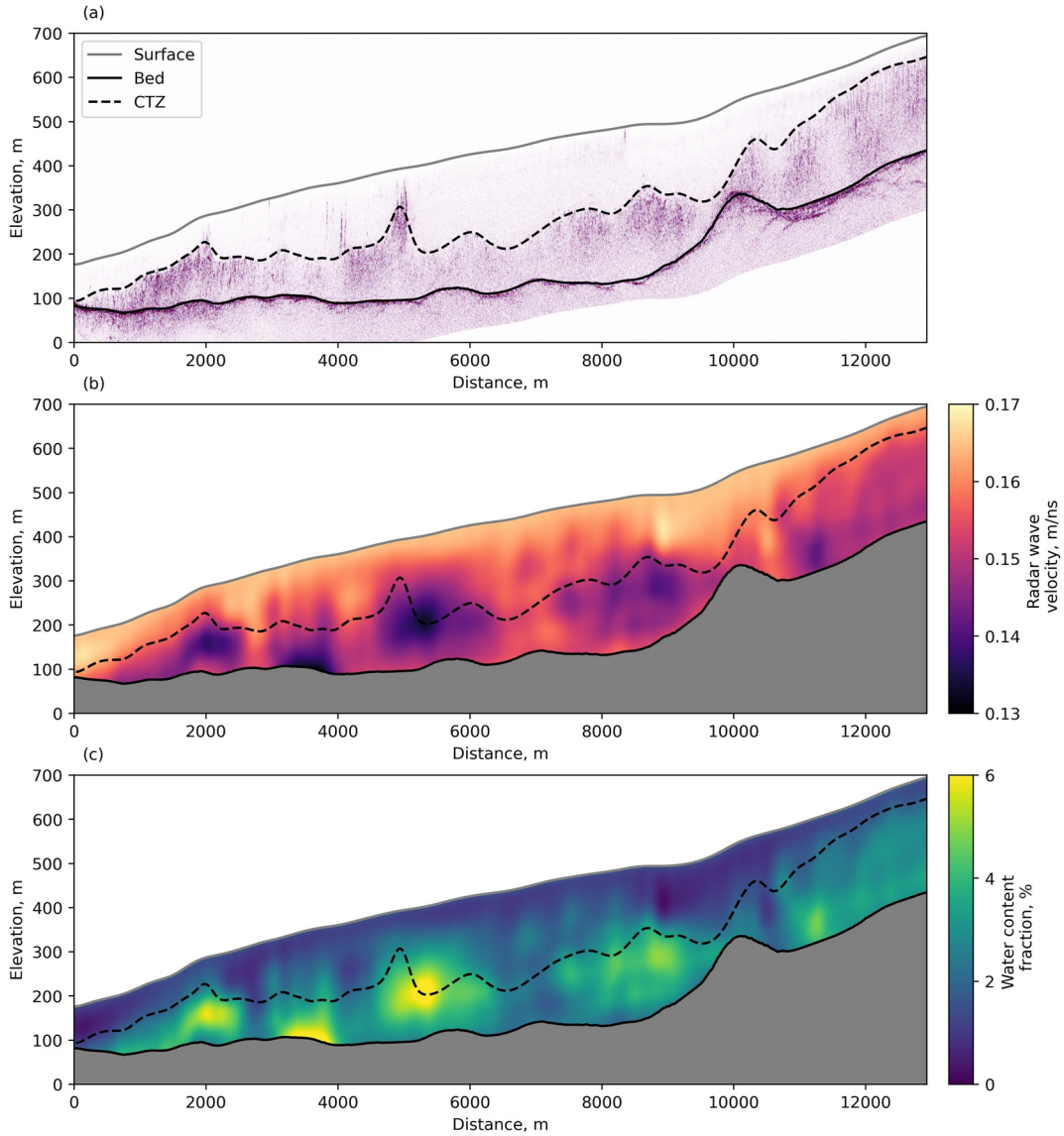

Figure 7. (a) Elevation-corrected centerline radar profile through Von Postbreen assuming constant englacial velocity of 0.165 m/ns. Dashed black line marks manually picked cold/temperate-ice transition zone (CTZ). Data are presented after pre-processing and singular value decomposition filtering. (b) Englacial velocity field derived by diffraction focusing. (c) Englacial water-content derived from the velocity field in panel (b), using Equations 10 and 11.

to complete the annual runoff and mass balance budget of Midre Lovenbreen, a smaller polythermal glacier with a low relative proportion of temperate ice by depth (Sevestre et al., 2015).

The presence of enhanced scattering through much of the region immediately below the CTZ may indicate a low hydraulic connectivity with the deeper subglacial hydrological network. At several locations in Figure 7, the inferred water content close to the bed is lower than in the overlying mid-ice column (for example, at approximately 2, 6, and 8 km in Figures 7b and 7c). Such a multi-layer structure has previously been observed using temperature profile measurements (Jania et al., 1996) and from GPR CMP velocity analysis (Murray et al., 2000), both inferring a 4-layer structure with temperate ice of water content of $3-5\%$ overlying a low water content region close to the bed. Our results partly follow this structure, but not continuously throughout the glacier, breaking down in some regions of low scattering intensity (e.g., at 7 km in Figure 7b). The wider variations in water content imply that the glacier thermal structure may not be well-represented by sparse CMP-derived estimates of 1D velocity profiles.

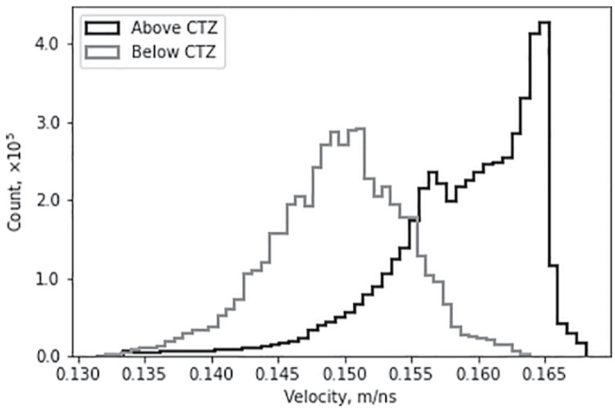

Figure 8. Histogram of derived local velocities observed above and below the manually interpreted cold-temperate ice transition zone, labeled as the clear layer and scattering layer, respectively.

5.2. The Nature of Scattering Bodies

Having elected to use the CRIM methodology of calculating englacial water content (Bradford et al., 2009; Brown et al., 2017), we assumed a 3-phase isotropic internal structure of englacial water content. The precise nature of englacial water is likely to be more complex than this. Some previous studies have assumed that water held within ice does so within intra-ice crystal veins, yet time-domain reflectometry of temperate glacier ice cores has shown that such veins only have a low capacity to store water, with an inferred upper bound of storage of <0.03% at 2° (West et al., 2007). Much water has instead been hypothesized to be stored predominantly in hydraulically disconnected macroscale pores, or voids, such as those imaged in the upper temperate ice of Storglaciaren using borehole video (Fountain et al., 2005). There, the majority of water storage and flow was found to be through fractures in the lower regions of ice, generally in the form of subglacial crevasses, at a similar orientation to the surface strain-related features and at sub-vertical (>70°) angles. This is consistent with Bradford et al. (2013), who showed through azimuthal GPR CMP surveys that velocity anisotropy is possible close to the bed of the glacier as a result of such subglacial features. Velocity anisotropy can be described by the retrieval of two dielectric constants parallel and perpendicular to the fracture orientation, known as $\epsilon_{\parallel}$ and $\epsilon_{\perp}$, respectively. This approach suggests an anisotropic mixing model should be used, for example, as developed by Giordano (2005), which enables estimation of a $\epsilon_{\perp}$ and $\epsilon_{\parallel}$ for a distribution or arbitrarily oriented bodies of defined aspect ratio.

We can test for anisotropy by considering the differences in twtt at survey line crossovers. Our survey grid gives a total of 16 crossover locations, with 8 at near-perpendicular and 8 at approximately 50° intersection angles. Figure 11 shows the results of crossover analysis on depth-converted data for all 16 locations using both constant and picked velocity fields. While all of the intersections are derived from regions with very small variations in bed topography, two outliers are present (highlighted in the constant-velocity plot of Figure 11), which are the result of slight cross-line variations in topography, resulting in a twtt bias. Our results show very little anisotropy at radar line crossover points. Average mis-tie between crossovers for data with constant velocity migration applied is 16 ± 32 ns, with all mis-ties below 61 ns, showing no systematic bias, suggesting a low anisotropy between orientations. This implies that water may be held

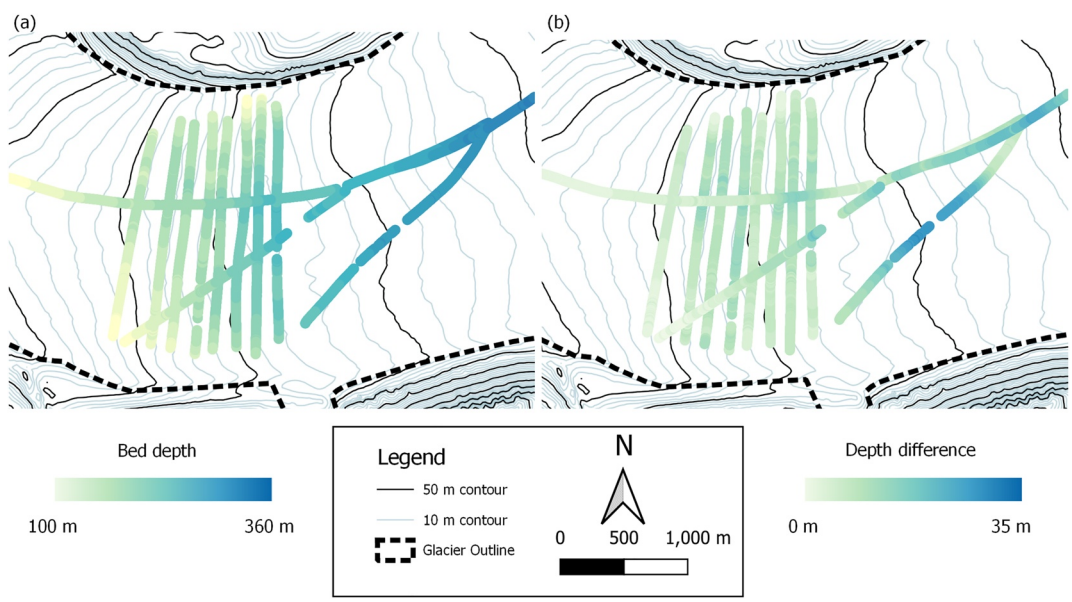

Figure 9. (a) Bed depth estimated using the diffraction-focusing velocity field over the main survey area. (b) Difference between bed topography using depths estimated with a constant velocity $v = 0.166$ m/ns minus depths using diffraction-focusing-derived V_{RMS}.

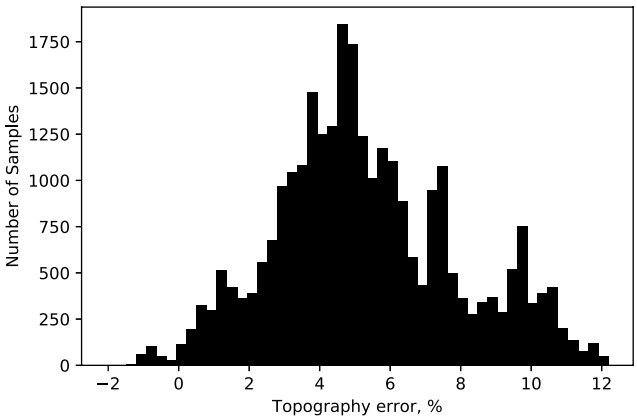

Figure 10. Histogram of percent error between constant velocity $v = 0.166$ m/ns) and picked velocity-derived bed topography.

in three possible configurations: (a) within macroscopic, disconnected pores, as predicted by West et al. (2007), with isotropic behavior, (b) within a series of subglacial fractures with a near-random distribution relative to the survey line such that the bulk dielectric constant has no azimuthal variation, or c), within fractures intersecting the survey lines by ≈45° such that $\epsilon_{\parallel} \approx \epsilon_{\perp}$. Of these, (a) would support use of a spherical inclusion mixing model such as Looyenga or the CRIM model, and (b) and (c) would support treating the inclusions as fractures or disks as in Giordano (2005) with different distributions of orientations. Of these, (b) is unlikely as crevasses will generally be uniform in orientation (perpendicular to the direction of bulk ice deformation after Cuffey and Paterson (2010)), and (c) is unlikely given that anisotropy is not observed for profiles intersecting at both ∼90° and ∼50°. Brown et al. (2017) interpret a similar result with TMz (parallel antennas) and TEz (perpendicular antennas) oriented common offset surveys in Greenland, and as such use isotropic mixing models. Air voids or pockets are unlikely to be a source of scattering within the deeper ice as they would be likely to close rapidly due to overburden pressure (Cuffey & Paterson, 2010), and scattering is unlikely to be debris-induced due to the lack of surface debris.

5.3. Radar-Wave Velocity and Bed Topography

Our derived velocity structure results in a consistently reduced bed depth compared to the assumption of a cold ice glacier with a velocity of 0.166 mns^{-1} (Figure 9). This is expected in the sense that other authors have shown bed depths can be overestimated when assuming constant englacial velocities in polythermal ice (e.g., Murray et al., 2000). For many such glaciers, a practical workaround has been to assume that high radio-wave velocities in the firn counteract the lower radio-wave velocities through the temperate ice, such that a constant velocity can be applied in most instances (Jania et al., 2005; Navarro et al., 2014). While absolute glacier volume estimates are within a suitable error range using this approach (Lapazaran et al., 2016), the relative error in bed depth along the glacier profile remains unconstrained, resulting in possible underestimates where firn/cold ice dominates and overestimates in regions of predominantly temperate ice. The effect of such a systematic error is unclear when mass-conservation approaches to glacier volume estimation are used, such as in retrieving archipelago-wide bed topography estimates in Svalbard by Fürst et al. (2018). Our data from Von Postbreen show a consistently lower velocity due to temperate ice through the full accumulation zone ice depth, similar to previous observations at this site (Sevestre et al., 2015), in addition to Kongsvegen (Björnsson et al., 1996) and Hansbreen (Jania et al., 2005). As such, we cannot assume that the higher velocities expected within snow and firn will be sufficient to counter low velocities of temperate ice.

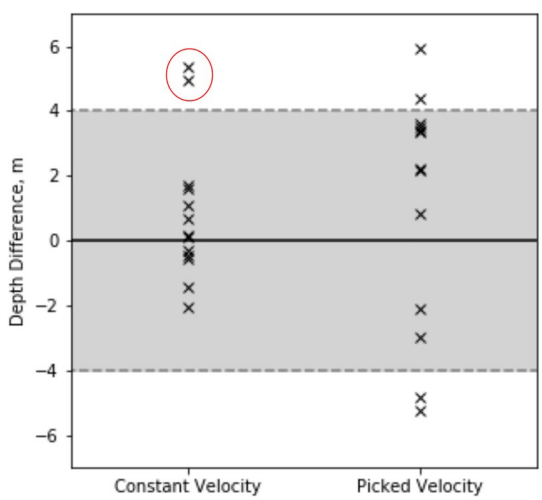

Figure 11. Scatter plot showing the difference between picked bed depth using a constant and picked velocity. This is calculated by $d_{\parallel} - d_{\perp}$, where $d_{\parallel}$ is the depth derived from surveys along flow and $d_{\perp}$ is derived from lines perpendicular to flow. Gray dashed lines show the average depth uncertainty, derived from the global average depth uncertainty.

6. Conclusions

We have applied a novel approach to estimate the radar wave velocity within polythermal glaciers to derive a continuous profile of englacial water content. We have achieved this by firstly extracting the diffracted wavefield using a coherent diffraction extraction technique, followed by automated extraction of diffraction focusing velocities. This study represents the first such automated approach to this problem, building on previously developed manual approaches. The quantification of englacial water content has for the most part relied on the use of common mid-point or common source-point surveys, which are logistically challenging, hence only a sparse representation of spatially variant glacier-wide water content distribution can be achieved. Common-offset data are far more readily available, and can be acquired over a sufficient spatial scale to well-represent the glacier-wide distribution of water content.

We find that the velocities derived using this approach typically result in ice depths which are lower than those obtained using a commonly assumed constant velocity, with an average difference of 4.9 ± 2.5% of local ice depth, or 12.0 ± 8.4 m in absolute terms, for data collected over Von Postbreen. We have shown that the spatial distribution of low radar-wave velocity regions, and the corresponding volumetric contributions of englacial water content, are more complex than can be described by interpretation of the CTZ alone. For example, regions of high englacial water content can be found in the vicinity of near-surface scatter, which may represent enhanced local melt or seasonal storage. We have demonstrated that understanding lateral variations of englacial radar velocity is essential, and that diffraction focusing and velocity estimation are crucial in retrieving correct bed topography in the presence of temperate ice. The workflow developed for this paper provides a mechanism for capturing these englacial radar velocity variations that, with careful tuning of scale factors in the velocity picking and smoothing stages, can be applied to GPR data acquired from diverse radar systems and survey settings.

Data Availability Statement

GPR data and Madagascar software codes associated with this research are available at https://doi.org/10.5281/zenodo.5148388. Radar data associated with this publication are available at https://doi.org/10.5281/zenodo.5148389.

Acknowledgments
R. Delf and R. G. Bingham acknowledge funding from the UK's Natural Environment Research Council via R. Delf's scholarship in the Edinburgh E^3 Doctoral Training Partnership (NE/L002558/1). Fieldwork was funded by the Svalbard Integrated Arctic Earth Observation System project 2017_0016. The authors thank the UNIS Tech and Logistics team for fieldwork support in Longyearbyen. The authors thank the NERC Geophysical Equipment Facility for supplying the GPR and GNSS equipment (Loan 1094) and invaluable advice through the project. B. Schwarz is grateful to Karin Sigloch, Tarje Nissen-Meyer, and Lotte Krawczyk for crucial support. We would like to thank Olga Sergienko and Paul Winberry for their handling of this article, and Seth Campbell, Scott Braddock, Emma Erwin, and two anonymous reviewers for their comments.

References

Arcone, S. A., Lawson, D. E., & Delaney, A. J. (1995). Short-pulse radar wavelet recovery and resolution of dielectric contrasts within englacial and basal ice of Matanuska Glacier, Alaska, USA. *Journal of Glaciology*, *41*(137), 68–86. https://doi.org/10.1017/S0022143000017779

Bamber, J. L. (1987). Internal reflecting horizons in Spitsbergen glaciers. *Annals of Glaciology*, *9*, 5–10. https://doi.org/10.3189/S0260305500200682

Barrett, B. E., Murray, T., & Clark, R. (2007). Errors in radar CMP velocity estimates due to survey geometry, and their implication for ice water content estimation. *Journal of Environmental & Engineering Geophysics*, *12*(1), 101–111. https://doi.org/10.2113/JEEG12.1.101

Benjumea, B., Macheret, Y. Y., Navarro, F. J., & Teixido, T. (2003). Estimation of water content in a temperate glacier from radar and seismic sounding data. *Annals of Glaciology*, *37*, 317–324. https://doi.org/10.3189/172756403781815924

Björnsson, H., Gjessing, Y., Hamran, S.-E., Hagen, J. O., LiestøL, O., Pálsson, F., & Erlingsson, B. (1996). The thermal regime of sub-polar glaciers mapped by multi-frequency radio-echo sounding. *Journal of Glaciology*, *42*(140), 23–32. https://doi.org/10.3189/S0022143000030495

Blatter, H., & Hutter, K. (1991). Polythermal conditions in arctic glaciers. *Journal of Glaciology*, *37*(126), 261–269. https://doi.org/10.3189/s0022143000007279

Booth, A. D., Clark, R., & Murray, T. (2010). Semblance response to a ground-penetrating radar wavelet and resulting errors in velocity analysis. *Near Surface Geophysics*, *8*(3), 235–246. https://doi.org/10.3997/1873-0604.2010008

Booth, A. D., Clark, R. A., & Murray, T. (2011). Influences on the resolution of GPR velocity analyses and a Monte Carlo simulation for establishing velocity precision. *Near Surface Geophysics*, *9*(1802), 399–411. https://doi.org/10.3997/1873-0604.2011019

Booth, A. D., & Pringle, J. K. (2016). Semblance analysis to assess GPR data from a five-year forensic study of simulated clandestine graves. *Journal of Applied Geophysics*, *125*, 37–44. https://doi.org/10.1016/j.jappgeo.2015.11.016

Bradford, J. H. (2005). Wave field migration as a tool for estimating spatially continuous radar velocity and water content in glaciers. *Geophysical Research Letters*, *32*(8), L08502. https://doi.org/10.1029/2004GL021770

Bradford, J. H., Nichols, J., Harper, J. T., & Meierbachtol, T. (2013). Compressional and EM wave velocity anisotropy in a temperate glacier due to basal crevasses, and implications for water content estimation. *Annals of Glaciology*, *54*(64), 168–178. https://doi.org/10.3189/2013AoG64A206

Bradford, J. H., Nichols, J., Mikesell, T. D., & Harper, J. T. (2009). Continuous profiles of electromagnetic wave velocity and water content in glaciers: An example from Bench Glacier, Alaska, USA. *Annals of Glaciology*, *50*(51), 1–9. https://doi.org/10.3189/172756409789097540

Brown, J., Harper, J., & Humphrey, N. (2017). Liquid water content in ice estimated through a full-depth ground radar profile and borehole measurements in western Greenland. *The Cryosphere*, *11*(1), 669–679. https://doi.org/10.5194/tc-11-669-2017

Copland, L., & Sharp, M. (2001). Mapping thermal and hydrological conditions beneath a polythermal glacier with radio-echo sounding. *Journal of Glaciology*, *47*(157), 232–242. https://doi.org/10.3189/172756501781832377

Cuffey, K., & Paterson, W. (2010). *The physics of glaciers* (4th ed.). Elsevier Science.

Daniels, D. J. (2004). *Ground penetrating radar* (2nd ed.). Institution of Electrical Engineers.

De Geer, G. (1910). A geological excursion to central Spitzbergen. In *Xie congres geologique international, stockholm, 1910 guide de l'excursion au spitzberg*. Norstedt.

De Vries, D., & Berkhout, A. J. (1984). Velocity analysis based on minimum entropy. *Geophysics*, *49*(12), 2132–2142. https://doi.org/10.1190/1.1441629

Dix, C. (1955). Seismic velocities from surface measurements. *Geophysics*, *120*, 68–86. https://doi.org/10.1190/1.1438126

Dowdeswell, J., Drewry, D., Liestøl, O., & Orheim, O. (1984). Airbourne radio echo sounding of sub-polar glaciers in Spitsbergen. In *Norsk polarinstitutt skrifter*. Norsk Polarinstitutt.

Dowdeswell, J. A., Hamilton, G. S., & Hagen, J. O. (1991). The duration of the active phase on surge-type glaciers: Contrasts between Svalbard and other regions. *Journal of Glaciology*, *37*(127), 388–400. https://doi.org/10.3189/S0022143000005827

Drewry, D. J., Liestøl, O., Neal, C. S., Orheim, O., & Wold, B. (1980). Airborne radio echo sounding of glaciers in Svalbard. *Polar Record*, *20*(126), 261. https://doi.org/10.1017/S0032247400003405

Farnsworth, W. R., Ingólfsson, Ó., Retelle, M., & Schomacker, A. (2016). Over 400 previously undocumented Svalbard surge-type glaciers identified. *Geomorphology*, *264*, 52–60. https://doi.org/10.1016/J.GEOMORPH.2016.03.025

Flink, A. E., Noormets, R., Kirchner, N., Benn, D. I., Luckman, A., & Lovell, H. (2015). The evolution of a submarine landform record following recent and multiple surges of Tunabreen glacier, Svalbard. *Quaternary Science Reviews*, *108*, 37–50. https://doi.org/10.1016/J.QUASCIREV.2014.11.006

Fomel, S. (2003). Time-migration velocity analysis by velocity continuation. *Geophysics*, *68*(5), 1662–1672. https://doi.org/10.1190/1.1620640

Fomel, S. (2007). Shaping regularization in geophysical-estimation problems. *Geophysics*, *72*(2), R29–R36. https://doi.org/10.1190/1.2433716

Fomel, S., Landa, E., & Taner, M. T. (2007). Poststack velocity analysis by separation and imaging of seismic diffractions. *Geophysics*, *72*(6), U89–U94. https://doi.org/10.1190/1.2781533

Forte, E., Dossi, M., Pipan, M., & Colucci, R. R. (2014). Velocity analysis from common offset GPR data inversion: Theory and application to synthetic and real data. *Geophysical Journal International*, *197*(3), 1471–1483. https://doi.org/10.1093/gji/ggu103

Fountain, A. G., Jacobel, R. W., Schlichting, R., & Jansson, P. (2005). Fractures as the main pathways of water flow in temperate glaciers. *Nature*, *433*(7026), 618–621. https://doi.org/10.1038/nature03296

Freire, S. L. M., & Ulrych, T. J. (1988). Application of singular value decomposition to vertical seismic profiling. *Geophysics*, *53*(6), 778–785. https://doi.org/10.1190/1.1442513

Fürst, J. J., Navarro, F., Gillet-Chaulet, F., Huss, M., Moholdt, G., Fettweis, X., et al. (2018). The ice-free topography of Svalbard. *Geophysical Research Letters*, *45*(21), 11760–11769. https://doi.org/10.1029/2018GL079734

Giordano, S. (2005). Order and disorder in heterogeneous material microstructure: Electric and elastic characterisation of dispersions of pseudo-oriented spheroids. *International Journal of Engineering Science*, *43*(13–14), 1033–1058. https://doi.org/10.1016/j.ijengsci.2005.06.002

Grab, M., Bauder, A., Ammann, F., Langhammer, L., Hellmann, S., Church, G. J., et al. (2018). Ice volume estimates of Swiss glaciers using helicopter-borne GPR – An example from the Glacier de la Plaine Morte. In *2018 17th international conference on ground penetrating radar, GPR 2018*. Institute of Electrical and Electronics Engineers Inc. https://doi.org/10.1109/ICGPR.2018.8441613

Greaves, R. J., Lesmes, D. P., Lee, J. M., & Toksöz, M. N. (1996). Velocity variations and water content estimated from multi-offset, ground-penetrating radar. *Geophysics*, *61*(3), 683–695. https://doi.org/10.1190/1.1443996

Gusmeroli, A., Murray, T., Jansson, P., Pettersson, R., Aschwanden, A., & Booth, A. D. (2010). Vertical distribution of water within the polythermal Storglaciären, Sweden. *Journal of Geophysical Research*, *115*(F4), F04002. https://doi.org/10.1029/2009JF001539

Hambrey, M. J., Murray, T., Glasser, N. F., Hubbard, A., Hubbard, B., Stuart, G., et al. (2005). Structure and changing dynamics of a polythermal valley glacier on a centennial timescale: Midre Lovenbreen, Svalbard. *Journal of Geophysical Research*, *110*(1), F01006. https://doi.org/10.1029/2004JF000128

Hamran, S., Aarholt, E., Hagen, J. O., & Mo, P. (1996). Estimation of relative water content in a sub-polar glacier using surface-penetration radar. *Journal of Glaciology*, *42*(142), 533–537. https://doi.org/10.3189/S0022143000003518

Hodson, A., Kohler, J., Brinkhaus, M., & Wynn, P. (2005). Multi-year water and surface energy budget of a high-latitude polythermal glacier: Evidence for overwinter water storage in a dynamic subglacial reservoir. *Annals of Glaciology*, *42*, 42–46. https://doi.org/10.3189/172756405781812844

How, P., Schild, K. M., Benn, D. I., Noormets, R., Kirchner, N., Luckman, A., et al. (2019). Calving controlled by melt-under-cutting: Detailed calving styles revealed through time-lapse observations. *Annals of Glaciology*, *60*, 1–31. https://doi.org/10.1017/aog.2018.28

Irvine-Fynn, T., Hodson, A. J., Moorman, B. J., Vatne, G., & Hubbard, A. L. (2011). Polythermal glacier hydrology: A review. *Reviews of Geophysics*, *49*(4), RG4002. https://doi.org/10.1029/2010RG000350

Irvine-Fynn, T., Moorman, B. J., Williams, J. L., & Walter, F. S. (2006). Seasonal changes in ground-penetrating radar signature observed at a polythermal glacier, Bylots Island, Canada. *Earth Surface Processes and Landforms*, *31*(7), 892–909. https://doi.org/10.1002/esp.1299

Jania, J., Macheret, Y., Navarro, F., Glazovsky, A., Vasilenko, E., Lapazaran, J., et al. (2005). Temporal changes in the radiophysical properties of a polythermal glacier in Spitsbergen. *Annals of Glaciology*, *42*, 125–134. https://doi.org/10.3189/172756405781812754

Jania, J., Mochnacki, D., & Gdek, B. (1996). The thermal structure of Hansbreen, a tidewater glacier in southern Spitsbergen, Svalbard. *Polar Research*, *15*(1), 53–66. https://doi.org/10.3402/polar.v15i1.6636

König, M., Nuth, C., Kohler, J., Moholdt, G., & Pettersen, R. (2014). A digital glacier database for Svalbard. In *Global land ice measurements from space* (pp. 229–239). Springer Berlin Heidelberg. https://doi.org/10.1007/978-3-540-79818-7_10

Langhammer, L., Rabenstein, L., Schmid, L., Bauder, A., Grab, M., Schaer, P., & Maurer, H. R. (2019). Glacier bed surveying with helicopter-borne dual-polarization ground-penetrating radar. *Journal of Glaciology*, *65*(249), 123–135. https://doi.org/10.1017/jog.2018.99

Lapazaran, J., Otero, J., Martín-español, A., & Navarro, F. (2016). On the errors involved in ice-thickness estimates I: Ground-penetrating radar measurement errors. *Journal of Glaciology*, *62*(236), 1008–1020. https://doi.org/10.1017/jog.2016.93

Macheret, Y. Y., Moskalevsky, M. Y., & Vasilenko, E. (1993). Velocity of radio waves in glaciers as an indicator of their hydrothermal state, structure and regime. *Journal of Glaciology*, *39*(132), 373–384. https://doi.org/10.3189/S0022143000016038

Madagascar. (2021). Madagascar software, version 3.2. www.ahay.org

Moore, J., Pälli, A., Ludwig, F., Blatter, H., Jania, J., Gadek, B., et al. (1999). High-resolution hydrothermal structure of Hansbreen, Spitsbergen, mapped by ground-penetrating radar. *Journal of Glaciology*, *45*(151), 524–532. https://doi.org/10.3189/S0022143000001386

Murray, T., Booth, A., & Rippin, D. M. (2007). Water-content of glacier-ice: Limitations on estimates from velocity analysis of surface ground-penetrating radar surveys. *Journal of Environmental & Engineering Geophysics*, *12*(1), 87–99. https://doi.org/10.2113/JEEG12.1.87

Murray, T., Gooch, D. L., & Stuart, G. W. (1997). Structures within the surge front at Bakaninbreen, Svalbard, using ground-penetrating radar. *Annals of Glaciology*, *24*, 122–129. https://doi.org/10.3189/S0260305500012040

Murray, T., Stuart, G. W., Fry, M., Gamble, N. H., & Crabtree, M. D. (2000). Englacial water distribution in a temperate glacier from surface and borehole radar velocity analysis. *Journal of Glaciology*, *46*(154), 389–398. https://doi.org/10.3189/172756500781833188

Norwegian Polar Institute. (2014). *Terrengmodell Svalbard (S0 Terrengmodell)*. https://doi.org/10.21334/npolar.2014.dce53a47

Navarro, F. J., Macheret, Y. Y., & Benjumea, B. (2005). Application of radar and seismic methods for the investigation of temperate glaciers. *Journal of Applied Geophysics*, *57*(3), 193–211. https://doi.org/10.1016/j.jappgeo.2004.11.002

Navarro, F. J., Martín-Español, A., Lapazaran, J. J., Grabiec, M., Otero, J., Vasilenko, E. V., & Puczko, D. (2014). Ice volume estimates from ground-penetrating radar surveys, Wedel Jarlsberg land glaciers, Svalbard. *Arctic Antarctic and Alpine Research*, *46*(2), 394–406. https://doi.org/10.1657/1938-4246-46.2.394

Neidell, N. S., & Taner, M. T. (1971). Semblance and other coherency measures for multichannel data. *Geophysics*, *36*(3), 482–497. https://doi.org/10.1190/1.1440186

Nicolson, H., Curtis, A., & Baptie, B. (2014). Rayleigh wave tomography of the British Isles from ambient seismic noise. *Geophysical Journal International*, *198*(2), 637–655. https://doi.org/10.1093/gji/ggu071

Pettersson, R., Jansson, P., & Blatter, H. (2004). Spatial variability in water content at the cold-temperate transition surface of the polythermal Storglaciären, Sweden. *Journal of Geophysical Research: Earth Surface*, *109*(F2). https://doi.org/10.1029/2003JF000110

Preine, J., Benjamin, S., Bauer, A., & Hübscher, C. (2020). When there is no offset – A demonstration of seismic diffraction imaging and depth-velocity model building in the southern Aegean Sea. *JGR Solid Earth*, *125*. https://doi.org/10.1029/2020JB019961

Saintenoy, A., Friedt, J.-M., Booth, A. D., Tolle, F., Bernard, E., Laffly, D., et al. (2013). Deriving ice thickness, glacier volume and bedrock morphology of Austre Lovénbreen (Svalbard) using GPR. *Near Surface Geophysics*, *11*(2), 253–262. https://doi.org/10.3997/1873-0604.2012040

Schannwell, C., Murray, T., Kulessa, B., Gusmeroli, A., Saintenoy, A., & Jansson, P. (2014). An automatic approach to delineate the cold–temperate transition surface with ground-penetrating radar on polythermal glaciers. *Annals of Glaciology*, *55*(67), 89–96. https://doi.org/10.3189/2014AoG67A102

Schwarz, B. (2019). Coherent wavefield subtraction for diffraction separation. *Geophysics*, *84*(3), V157–V168. https://doi.org/10.1190/geo2018-0368.1

Schwarz, B., & Gajewski, D. (2017). Accessing the diffracted wavefield by coherent subtraction. *Geophysical Journal International*, *211*(1), 45–49. https://doi.org/10.1093/gji/ggx291

Sevestre, H., Benn, D. I., Hulton, N. R. J., & Baelum, K. (2015). Thermal structure of Svalbard glaciers and implications for thermal switch models of glacier surging. *Journal of Geophysical Research: Earth Surface*, *120*(10), 2220–2236. https://doi.org/10.1002/2015JF003517

Shannon, C. E. (1948). A mathematical theory of communication. *Bell System Technical Journal*, *27*(3), 379–423. https://doi.org/10.1002/j.1538-7305.1948.tb01338.x

Storn, R., & Price, K. (1997). *Differential evolution – A simple and efficient heuristic for global optimization over continuous spaces* (Techniocal Report, Vol. 11). https://doi.org/10.1023/a:1008202821328

Stuart, G. (2003). Characterization of englacial channels by ground-penetrating radar: An example from Austre Brøggerbreen, Svalbard. *Journal of Geophysical Research*, *108*(B11), 2525. https://doi.org/10.1029/2003JB002435

Sweeting, M., & Groom, G. (1956). Notes on the glacier fluctuations in Bünsow Land, central Vestspitsbergen. *Journal of Glaciology*, *2*(19), 640–641. https://doi.org/10.3189/002214356793701875

Toldi, J. L. (1989). *Velocity analysis without picking* (Technical Report No. 2, Vol. 54). https://doi.org/10.1190/1.1442643

West, L., Rippin, D. M., Murray, T., Mader, H. M., & Hubbard, B. (2007). Dielectric permittivity measurements on ice cores: Implications for interpretation of radar to yield glacial unfrozen water content. *Journal of Environmental & Engineering Geophysics*, *12*(1), 37–45. https://doi.org/10.2113/JEEG12.1.37

Yilmaz, Ö. (2001). Seismic data analysis. *Society of Exploration Geophysicists*. https://doi.org/10.1190/1.9781560801580